

22 episode (EP-2 and EP-4) featured as the low Aerosol Optical Depth (AOD = 0.72) and less
23 pollutants compared with haze (1.14) and fog (2.92) episodes ~~and the particles, which~~ are
24 mostly externally mixed. The high Ångström exponent (> 2.0) suggests that coarse particles
25 were scarcely observed in EP-2 due to the washout of a previous heavy rain, whereas they were
26 widespread in EP-4 (Ångström exponent = 0.04), which had some mineral particles introduced
27 from the north. In contrast, industry-induced haze (EP-1) and biomass burning-induced haze
28 (EP-5) were both affected by the south air mass. Compared with the EP-2 and EP-4, the AOD
29 values and the size distribution of particles during EP-1 and EP-5 were much greater because
30 of relatively high particle concentrations. All of the particles were classified into nine categories
31 including S-rich, N-rich, mineral, K-rich, soot, tar ball, organic, metal and fly ash on the basis
32 of TEM analysis. In the haze episode, In contrast to the EP-1, a large fraction of soot, which
33 sticks to KCl, sulphate or nitrate particles was detected during the EP-5~~as the influence of~~
34 ~~severe crop residue combustion, a large fraction of soot was detected, which sticks to sulphate~~
35 ~~or nitrate particles transformed from KCl.~~ Additionally, evident enhancement of light
36 absorption was observed during the EP-5, which was mainly ascribed to both BC acceleration
37 and other absorbing substances.~~The light absorption enhancement was contributed by both~~
38 ~~black carbon (BC) acceleration, internally mixed effects, and other light absorbing substances.~~
39 However, soot was found mostly internally mixed with sulphate and nitrate during a soot fog
40 episode (EP-3), resulting in evident enhancement of light absorption~~For foggy days, soot was~~
41 ~~mostly internally mixed with sulphates and nitrates, which revealed themselves after electron~~
42 ~~exposure under the TEM.~~ The larger size distribution was likely to be caused by both

43 hygroscopic growth and collision between particles during the aging. About 28% of particles
44 were internally mixed in the foggy days, which favored the light absorption. The comparison
45 of all the episodes provides a deeper insight of how mixing states influence the aerosol
46 extinction properties and also a clue to the air pollution control in the crop burning seasons.

47 **Keywords:**

48 Aerosol optical depth, Ångström exponents, Single scattering albedo, Transmission Electron
49 Microscope, Biomass burning, Soot

50 **1. Introduction**

51 Aerosol particles are ubiquitous in the troposphere and exert an important influence on global
52 climate and the environment (Ramana et al., 2010). They affect climate through direct
53 scattering, transmission, and absorption of radiation, or indirectly by acting as nuclei for cloud
54 formation (Buseck and Posfai, 1999). In addition, light extinction by aerosol particles can
55 impair visibility, both during extreme events such as dust storms, and more widely in the
56 vicinity of urban regions, frequently leading to regional haze and fog events (Wang et al., 2009a;
57 Chameides et al., 1999; Sun et al., 2006; [Salch et al., 2016](#)). ~~Common scattering aerosols in the~~
58 ~~atmosphere include inorganic~~ Inorganic salts and light-color organic carbon. ~~These aerosols~~
59 have ~~mainly~~ a “cooling effect” on the climate due to a decrease in the solar radiation that reaches
60 the Earth’s surface (Buseck and POsfai, 1999). Soot aerosols, mineral dust, and brown carbon
61 are important absorbing aerosols that can lead to global and regional warming effects (Buseck
62 and POsfai, 1999; Bahadur et al., 2012; Wang et al., 2014). The impact of aerosols on the Earth’s

63 climate is a major uncertainty in climate change models as was emphasized in the latest
64 Intergovernmental Panel on Climate Change (IPCC) report (Solomon, 2007). It follows that
65 understanding aerosol optical behaviour and associated spatial and temporal variability is a
66 necessary prerequisite to understanding its role in climate and the environment (Langridge et
67 al., 2012;Che et al., 2014).

68 Soot is a major contributor to Earth's radiative balance (Ramana et al., 2010). Recent
69 investigations involving direct atmospheric measurements of soot aerosols suggest that they
70 may have a global warming potential second only to CO₂, and the warming effect by soot nearly
71 balances the net cooling effect of other anthropogenic aerosols (Jacobson, 2001). Not
72 surprisingly, the importance of soot to climate change has been a major focus of many
73 modelling, laboratory, and field studies (Zhang et al., 2008;Adler et al., 2010;Moffet and
74 Prather, 2009;Adachi and Buseck, 2008;Ram et al., 2012). The main uncertainty stems from
75 the fact that the actual amount soot warms our atmosphere strongly depends on the manner and
76 degree in which it is mixed with other species, a property referred to as mixing state (Jacobson,
77 2001;Moffet and Prather, 2009). The mixing state was found to affect the soot global direct
78 forcing by a factor of 2.9. It has been shown that absorption by soot increases when soot
79 particles are internally mixed and/or coated with other less absorbing materials (Moffet and
80 Prather, 2009). This enhanced absorption in such structure is because of the lensing effect of
81 coated materials (Jacobson, 2001). Field measurements indicate that during transport from the
82 sources, fresh soot becomes internally mixed with sulphate and organics, leading to
83 enhancement in light absorption, which confirms the modelling calculation (Kleinman et al.,

84 2007;Doran et al., 2007;Carabali et al., 2012). Kleinman et al. observed a doubling in the ratio
85 of aerosol light absorption in aged air masses compared to fresh emissions over the eastern U.S.
86 (Kleinman et al., 2007). Similar increases in absorption by soot-bearing aerosol have been
87 reported from ground site measurements performed at a series of locations downwind of
88 Mexico City (Doran et al., 2007). Compiling both the surface and aircraft measurements,
89 Ramana et al. recommended that the solar-absorption efficiency of the Beijing and Shanghai
90 plumes was positively correlated with the ratio of soot to sulphate (Ramana et al., 2010). Lei et
91 al. further confirmed that the enhanced absorption of mixed aerosols depended upon
92 hygroscopicity and the thickness of the coating (Lei et al., 2014). Based on the combined proof
93 from the modelling and field studies, most of researchers proposed that internal mixing models
94 of soot present more realistic absorption estimates as compared to external mixing models in
95 which soot particles coexist with other particles in a physically separated manner (Jacobson,
96 2001;Ramana et al., 2010;Lei et al., 2014).

97 Biomass burning is by far the largest source of primary, fine carbonaceous aerosols in the
98 atmosphere (Habib et al., 2008). It is estimated to contribute 20% of soot aerosols from biomass
99 burning. Besides strongly absorbing soot particles, high amounts of brown organic carbon, such
100 as “tar ball” or HULIS, can be emitted from biomass burning (Roden et al., 2006;Hand et al.,
101 2005;Hoffer et al., 2006). Brown carbon has a significant absorbing component at short
102 wavelengths that may be comparable to the soot absorption (Alexander et al., 2008;Bahadur et
103 al., 2012). Consequently, organic carbon from biomass burning may also contribute to the
104 warming potential of aerosols (Alexander et al., 2008). These large quantities of climate-related

105 aerosols can persist in the atmosphere for several weeks and be transported over long distances.
106 As a result, biomass burning aerosols have a significant impact on climate, which was
107 considered to provide a major uncertainty in accurately predicting the effects of light-absorbing
108 aerosols on the climate (Bahadur et al., 2012). Many field measurements in East Asia, South
109 Asia and Africa have shown extensive biomass burning in these regions causes important
110 perturbations to Earth's atmosphere (Gustafsson et al., 2009; Alexander et al., 2008; Hand et
111 al., 2005). Once biomass burning particles are mixed with other atmospheric components
112 during aging and transport, such as sulfate and dust, solar absorption is further amplified due
113 to the formation of internally mixed particles (Ramanathan et al., 2005). Such mixtures of
114 absorbing and scattering aerosols at the regional scale are referred to as ABCs, for atmospheric
115 brown clouds (Ramanathan et al., 2007). ABCs radiative forcing can cool the surface, stabilize
116 the atmosphere, and reduce evaporation and monsoonal rainfall. The large influence of ABCs
117 on the climate and hydrological cycle changes has recently been demonstrated through model
118 simulations (Ramanathan et al., 2007; Ramanathan et al., 2005).

119 In the farmlands of eastern China such as that near Beijing, most wheat straw is burned in
120 the field within one week after harvesting in preparation for rice cultivation during May and
121 June. Emissions from the biomass burning are often transported and mixed with urban pollution,
122 leading to degradation of air quality, visibility impairment, and regional haze events (Li et al.,
123 2010). Stagnation occurs during episodes of urban haze, when there is insufficient wind
124 velocity to carry pollutants away from the city (Katrinak et al., 1993; Sun et al., 2006). During
125 these periods of pollutant retention, haze particles aggregate continue to collide and combine,

126 resulting in larger average sizes and altered morphology (Li et al., 2010). Enhanced absorption
127 is mainly brought about in the presence of high levels of non-absorbing hygroscopic aerosols
128 such as sulphates, nitrates, and water-soluble organic carbon, as their hygroscopic nature favors
129 internal mixing/core-shell formation (Bahadur et al., 2012). On the other hand, under the
130 condition of high atmospheric relative humidity (RH), the initially hydrophobic soot particles
131 can become associated with hygroscopic materials, leading to increased scattering due to
132 particle growth. At an extreme case, the coating material can cause the absorbing fractal soot
133 to collapse, potentially changing optical behaviour, to further complicate this picture (Zhang et
134 al., 2008; Langridge et al., 2012; Lei et al., 2014; [Tan et al., 2016](#)). Such changes cause both
135 positive and negative effects on the interplay between the direct and indirect aerosol effects,
136 making overall prediction of the radiative forcing difficult. Up to date, large uncertainties exist
137 in estimates of the radiative forcing of haze particles because of the lack of detailed in situ
138 measurements of the mixing state and the associated optical properties as a function of particle
139 size and composition (Moffet and Prather, 2009). These uncertainties limit our ability to
140 quantify the relative impacts of soot on climate, thus limiting our ability to make effective
141 policy decisions.

142 In an attempt to address this knowledge gap, and in the absence of the opportunity for
143 widespread field studies in eastern China, the experiments in this study were designed to
144 simultaneously measure mixing states and optical properties of haze particles. The present
145 analysis focused on the Beijing plume, which in addition to strong urban emissions is
146 influenced by local agricultural emissions (Li et al., 2010). Light extinction and scattering

147 coefficient was measure with a cavity ring-down spectrometer (CRDs) and a nephelometer,
148 respectively. Absorption was calculated from the difference between extinction and scattering.
149 Individual aerosol particles were identified with transmission electron microscopy (TEM).
150 Back trajectory analyses suggest flow patterns consistent with long-range transport of
151 agricultural smoke to the study site during periods when the sampling site was engulfed by the
152 serious haze and fog.

153 **2. Experimental Sections.**

154 **2.1 site description**

155 All of ambient investigation of aerosol optical properties and TEM samplings were
156 conducted at the Institution of Atmospheric Physics (39°58'N, 116°22'N), Beijing, China, from
157 24th May to 22nd Jun, 2012. Samplers were mounted on the roof of a two-story building about
158 8 m above ground level. The surroundings are in the convergence of residential and commercial
159 zones with some steel plants locating around in a distance of 6 to 25 km and a waste incineration
160 facility (Gaodun) 8 km in the northeast, which has an operational capacity of 1600 t d⁻¹. In
161 addition, the sampling site is suited in the middle of the North Third Ring Road and North
162 Fourth Ring Road, approximately 360 m south and 380 m north, respectively. The sampling
163 site is impacted by the mixture of residential, industrial, waste combustion and vehicle
164 emissions, but not dominated by any one source.

165 **2.2 Cavity ring-down spectrometer and nephelometer**

166 A self-designed cavity ring-down spectrometer (CRDS) was performed to measure the
167 extinction coefficient of aerosols at 1 min intervals with an accuracy of 0.1 Mm⁻¹. Aerosols

带格式的: 非上标/ 下标

带格式的: 非上标/ 下标

168 were dried by diffusion drying tubes before they reached CRDS and Nephelometer to exclude
169 the influence of relative humidity (RH) on the aerosol optical properties. RH was kept below
170 40% to minimize the effects of changing RH on measurements. The cavity was formed by two
171 high-reflectivity dielectric mirrors (Los Gatos Research, Inc., Mountain View, CA, USA) and
172 a stainless steel cell equipped with two inlets at both ends and one outlet in the middle. The
173 entire distance of two mirrors is 76.4 cm, while the filling length is 58.0 cm. Dry nitrogen
174 was released near the mirrors at a flow of 0.03 L min⁻¹ to prevent the contamination of mirrors
175 and aerosol flow was set 1.0 L min⁻¹. The 532 nm light pulse (energy 100 μJ, duration 11 ns)
176 was generated by a Q-switched pulsed laser (CrystaLaser QG-532-500). Leaking light through
177 the mirrors was monitored by a Hamamatsu R928 photomultiplier. Details about the system
178 were reported by Li et al (2011). To calculate the decay time, 1000 ring-down traces were
179 averaged at 1000 Hz repetition rate. The extinction coefficient (α_{ext}) has an uncertainty below
180 3% under the controlled conditions. It was calculated according to the following equation:

181

$$\alpha_{ext} = \frac{L}{lc} \left(\frac{1}{\tau} - \frac{1}{\tau_0} \right) \quad (1)$$

182 Where L is the length of the cavity, l is effective length occupied by particles, c is the speed of light, τ_0
183 is ring-time time of the cavity filled with particle-free air and τ is the calculated decay time (Li et al.,
184 2011).

185 An integrating nephelometer (TSI, Model 3563) was operated to obtain aerosol scattering coefficient at
186 three different wavelengths (450, 550, and 700 nm) and the flow rate was set at 5 L min⁻¹. During the field
187 campaign, zero check was done automatically by pumping in particle-free air for 5 min once every 2 h, and
188 a span check was conducted manually using CO₂ as the high span gas and filtered air as the low span gas
189 every week. RH was kept below 40% to minimize the effects of changing RH on measurements (Peppler
190 et al., 2000; Clarke et al., 2007). The raw data were corrected for truncation errors and a non-Lambertian
191 light source using Ångström exponents (\hat{a}) according to Anderson and Ogren (1998) (Anderson and Ogren,
192 1998). Generally, the total uncertainty of the scattering coefficient (α_{scat}) was generally below 10%. In
193 accordance with the extinction coefficient at 532 nm, the scattering coefficients was
194 converted to 532 nm ($\alpha_{scat,532}$) on the basis of the following equation:

195

$$\alpha_{scat,532} = \alpha_{scat,\lambda} \left(\frac{532}{\lambda} \right)^{-\hat{a}} \quad (2)$$

196 Where $\alpha_{scat,\lambda}$ is the scattering coefficient at the wavelength of λ . Accordingly, \hat{a} could be computed
197 calculated as the equation (3),

198

$$\hat{a} = - \frac{\lg(\alpha_{scat,\lambda_1} / \alpha_{scat,\lambda_2})}{\lg(\lambda_1 / \lambda_2)} \quad (3)$$

199 and the single scattering albedo (ω_0) at the given wavelength could be calculated from equation (4),

200

$$\omega_0 = \frac{\alpha_{scat}}{\alpha_{ext}} \quad (4)$$

201 As the sum of absorption (α_{abs}) and scattering (α_{scat}) coefficients equals the extinction coefficient (α_{ext}),

202 α_{abs} could be derived from the equation (5),

203
$$\alpha_{abs} = \alpha_{ext} - \alpha_{scat} \quad (5)$$

204 It is known that RH also has a profound impact on visibility (Chow et al., 2002), however, in this study the
205 aerosols passed through a diffusion drying tube before the measurement of optical properties, thus aerosol
206 optical property measurements and TEM observations were both performed in dry condition.

207 **2.3 Aethalometer**

208 An Aethalometer (model AE-31, Magee Scientific Company) was employed to simultaneously quantify
209 BC concentration by calculating the optical attenuation (absorbance) of light from light emitting diode
210 lamps emitting at seven different wavelengths (370, 470, 520, 590, 660, 880 and 950 nm) every 5 minutes,
211 with a typical half-width of 0.02 μm (Hansen, 2003). The flow rate was set to be 5 L min^{-1} and a clean filter
212 canister in the inlet was used weekly to conduct the zero calibration. A $\text{PM}_{2.5}$ cyclone (BGI SCC 1.828)
213 was employed in the sampling line with a flow rate of 5 L min^{-1} . A typical noise level is less than 0.1 μg
214 cm^{-3} on a 5-min basis. Two photo-detectors monitor the light intensity as a function of time. One measured
215 the light intensity of the light crossing reference quartz filter, while the other measured that of the same
216 light crossing a sample spot under the identical conditions. The wavelength at 880 nm was used to derive
217 the aerosol absorption coefficient (σ_{abs}). Then BC concentration could be converted under the assumption
218 that the BC mass concentration [BC] on the filter was linearly correlated to the aerosol absorption
219 coefficient, as the following equation (6),

220
$$\sigma_{abs} = \alpha[\text{BC}] \quad (6)$$

221 Where [BC] is the BC mass concentration, and α is a conversion factor. A factor of 8.28 $\text{m}^2 \text{g}^{-1}$ was
222 employed to convert the aerosol absorption coefficient to BC concentration, according to the results of
223 inter-comparison experiment conducted in south China (Wu et al., 2009; Yan et al., 2008).

224 The uncertainty of measurement might originate from the multiple scattering in the filter fibres in the
225 unloaded filter and in those particles embedded in the filters (Clarke et al., 2007; Jeong et al., 2004). The

226 attenuation values were within the limit of an acceptable uncertainty, that is, no greater than 150 in the
227 range of 75-125 at various wavelengths, verifying the reliability of the measurement. Moreover, the BC
228 concentration was compared with the results of multi-angle absorption photometry (MAAP, Model-5012)
229 and a particle soot absorption photometer (PSAP, Radiance Research), which shows great consistence.

230 **2.4 Aerosol optical depth**

231 Aerosol optical depth (AOD) data at the sampling site was based on the MODIS (Moderate Resolution
232 Imaging Spectroradiometer) retrieved data from a CIMEL CE-318 sunphotometer (AERONET/PHOTONS)
233 at Institute of Atmospheric Physics, reflecting the amount of direct sunlight prevented from reaching the
234 ground by aerosol particles by measuring the extinction of the solar beam. The AOD value of the sampling
235 site was downloaded from the AERONET (<http://aeronet.gsfc.nasa.gov>), using the Level 2.0. Quality
236 Assured Data. These data are pre and post field calibrated, automatically cloud cleared and manually
237 inspected. The regional distribution of AOD was obtained from Giovanni (GES-DISC Interactive Online
238 Visualization And Analysis Infrastructure) maps from MODIS satellite data
239 (<http://disc.sci.gsfc.nasa.gov/giovanni>). Two continuous episodes featuring as clear and haze are chosen,
240 23th May to 27th May and 19th June to 27th June, respectively.

241 **2.5 TEM Analysis**

242 Samples were made by collecting air-borne particles onto copper TEM grids coated with carbon film
243 (carbon type-B, 300-mesh copper, Tianld Co., China) using a single-stage cascade impactor with a 0.5 mm
244 diameter jet nozzle at a flow rate of $1.0 \text{ L} \cdot \text{min}^{-1}$. According to the visibility, the sampling time varies from
245 1 min to 10 min. 3 or 4 samples were collected each morning at around 8 am and also each time when haze
246 or fog appeared. After collection, samples were stored in a dry plastic box sealed in a plastic bag and kept
247 in a desiccator at $25 \text{ }^\circ\text{C}$ and $20 \pm 3\%$. Details of the analysed samples, such as sampling time and
248 instantaneous meteorological state are listed in Table 1.

249 Individual aerosol samples were analysed using a high resolution TEM (JEOL 2010, Japan) operated at
250 200 kV. TEM can obtain morphology, size, and mixing state of individual aerosol particles. Energy-
251 dispersive X-ray spectrometer (EDS) can get the chemical compositions of the targeted particles. Cu and C

252 were excluded from the copper TEM grid with carbon film. Details have been described in the previous
253 paper (Fu et al., 2012; Guo et al., 2014a). Particle sizes on the grid decrease from the centre to the periphery
254 due to the limitation of sampler, and three to four round meshes were chosen from the centre to the periphery
255 in a line to ensure the representative of the entire size range. Each mesh analyses three to four views. The
256 average values of each mesh were used for statistics. The analysis was done by labour-intensive manual
257 sortation of the particles. 9 grids, all of 1173 particles have been analysed by TEM.

258 **2.6 Back trajectories and meteorological data**

259 NOAA/ARL Hybrid Single-Particle Lagrangian Integrated Trajectory model (available at
260 <http://www.arl.noaa.gov/ready/hysplit4.html>) was employed to determine back trajectories arriving at
261 Beijing at 100 m, employing the data of global data assimilation system (GDAS). Each trajectory
262 represented the past 72 h of the air mass, with its arrival time at 00:00 UTC every day.

263 Meteorological data was downloaded from Weather Underground (www.wunderground.com), and Daily
264 PM₁₀ values were transformed from daily API (Air Pollutant Index) in the datacentre of ministry of
265 Environmental Protection of the People's Republic of China (<http://datacenter.mep.gov.cn/>).

266 **3. Results and Discussion**

267 **3.1 Episode segregations**

268 Haze was usually defined as a weather phenomenon that lasts a duration of at least 4 h when the visibility
269 is less than 10 km and RH lower than 80% (Sun et al., 2006), while fog was characterized with a higher
270 RH, larger than 90%, according to the Chinese Meteorological Administration. The sampling period was
271 categorized into 5 episodes to observe the optical properties between different weather phenomena (Fig. 1).
272 Although every episode contains a mixture of different pollutions, the main origin can be discerned by
273 studying the weather condition, back trajectories and fire maps. The 1st episode (EP-1) was from 28th May
274 to 29th May, when a haze occurred with the south wind bringing in the industrial pollution from the heavily
275 polluted cities in the south, which conformed to the 3-day back trajectories shown in Fig. 2a, showing the
276 air masses passing through Henan, Shandong, Hebei and Tianjin before arriving at the sampling site. Only
277 scattered fire spots were observed during these days along the air mass pathway, suggesting little biomass

278 burning emission interference. The 2nd episode (EP-2) was in clear weather on 30th May. A heavy rain
279 interrupted the previous haze; hence the air were cleaned up by rain washout. It was impacted by the air
280 mass from the north region (Fig. 2b), as ~~the air parcel from the North was relatively clean-the north wind~~
281 ~~was relatively clean~~ and the time was insufficient for a heavy accumulation. This episode could be viewed
282 as the background. The 3rd episode (EP-3) from 31st May to 9th Jun was fickle, with a variety of transitions
283 between fog, haze and clear days. This was partly caused by the variable wind directions and air mass
284 transferring (Fig. 2c). When the wind is from east, the back trajectories are across the Bohai Sea, and the
285 air mass carries a high content of water vapour, facilitating the formation of fog, whereas when south wind
286 is dominant, haze is likely to occur (Wang and Chen, 2014;Zhang et al., 2010). The following 4th episode
287 (EP-4) from 10th Jun to 16th Jun is mainly clear days with slight dust. Their back trajectories originate
288 from the north part (Fig. 2d), and mostly travelling from the Siberian region, across eastern Mongolia and
289 Inner Mongolia and finally arriving the sampling site with little pollution. The last episode (EP-5) was from
290 17th Jun to 21st Jun. Severe haze was observed during this duration. Fig. 2e shows that the air parcel
291 pathway across by dense fire spots, indicating a severe impact of the biomass burning. Every year after
292 harvest, crop residue burning is extremely frequent in Anhui, Shandong and Henan provinces as they served
293 as important centres for the rice supply (Li et al., 2010). Therefore, the biomass burning emissions can be
294 the main contributor to the haze formation in this episode.

295 **3.2 The variation of aerosol optical characters**~~Optical parameter variation~~

296 Aerosol optical depth (AOD) is representative of the airborne aerosol loading in the atmospheric column,
297 which was also verified by a significant related coefficient with PM_{10} ($R_r=0.603$) (Fig. 1). The overall AOD
298 is contributed by both Mie scatter and Rayleigh scatter (Fig. 3a). The former one is produced by the scatter
299 effect of particles while the latter one by gases (Brown et al., 2014). The data shown in Fig. 1 demonstrates
300 that gas plays a negligible role in the AOD value, especially when aerosol loading is high. Apparently, the
301 AOD value varied with the weather transition. During the clean days, the mean AOD was 0.723, while it
302 became higher when the haze and fog were formed, with a mean value of 2.92 and 1.14, respectively.

303 During the measurement period, AOD reached its highest value of 5.0 in the hazy EP-5, which was much
304 higher by 5 times than the average AOD of 0.95 in Beijing measured from Mar 2012 to Feb 2013 (Guo et
305 al., 2014b). Such high AOD could be attributed to the pollutant accumulation, especially biomass burning
306 emission from the crop combustion.

307 Ångström exponent (\AA) is a good indicator of aerosol size distribution, which decreases with the increase
308 of particle size (Eck et al., 1999). The value is computed from pairs of AOD measurements at 700 nm with
309 450 nm, 700 nm with 550 nm and 550 nm with 450 nm, respectively. A high accordance is observed
310 between each pair (Fig. 3b). The \AA increases sharply to its highest value above 2.0 at EP-2, 45 times of the
311 minimum value 0.044 observed in EP-5. This could be explained by the wet removal impact of the heavy
312 rain. It is well known that rains wash out the coarse particles, resulting in a fine size distribution (Dey et al.,
313 2004). The \AA value during EP-4 fluctuated between 0.08 and 0.2. Since the rains are light and short, the
314 clear days in EP-4 are more impacted by the north air mass, which brings in a larger fraction of coarse dust
315 particles. Comparatively, the \AA value was lower in both the haze and fog periods including EP-1, EP-3 and
316 EP-5. Especially in the case of EP-5, the low \AA value indicated that the biomass burning emission could
317 contain more coarse particles. Such scene is in contrast to the conclusion that the haze days were dominated
318 by fine particles (Yan et al., 2008). It is likely caused by the high collision occurrences of fine particles
319 along the long-range transport from the fire spots (Wang et al., 2009b). In comparison, the \AA value during
320 2001 to 2005 in Beijing altered between 0.04 and 1.06 (Yu et al., 2006). The lower limit is similar with the
321 present field-measurement, while the upper limit is much higher than this study. This could be attributed to
322 the increase of fine particle emission contributed by more vehicles, waste incineration and industrial plants
323 in the past years.

324 Single scattering albedo (SSA), ω , was defined as the ratio of the aerosol scattering coefficient (σ_{sca}) to
325 the extinction coefficient (σ_{ext}). This parameter is especially important in the estimation of direct aerosol
326 radiative forcing, since even a small error in its estimation might change the sign of aerosol radiative forcing
327 (Takemura et al., 2002). Figs. 3c and d show the time series of σ_{sca} , σ_{abs} , σ_{ext} and SSA at 550 nm during the

328 measurement period. The mean ω was 0.73, 0.82 and 0.79 in EP-2, EP-4, and EP-5, respectively, implying
329 that mineral dust in EP-4 accelerates the optical scattering while soot favours the optical absorption.
330 Compared with other reported results (Che et al., 2014; Li et al., 2007; Qian et al., 2007), the mean ω is
331 lower in this study, suggesting that more soot is uploaded into the atmosphere during this period. It is well
332 known that soot emission is much higher in the past years, mainly contributed by the residential coal
333 combustion, biomass burning, coke production, and diesel vehicles (Wang et al., 2012b). Especially, when
334 air masses moved from south direction the sampling site were influenced by heavy polluted air mass mixed
335 by soot, sulfate, and OC-components, from the dense population centres and industrial areas (Sun et al.,
336 2006; Wang et al., 2006), which was also confirmed by the TEM observation.

337 **3.3 “Morphology and chemical composition of aerosols”-TEM analysis**

338 Based on morphology and chemical composition, 1173 particles were classified into nine categories: S-rich
339 (Fig. 4a), N-rich (Fig. 4b), mineral (Fig. 4c), K-rich (Fig. 4d), soot (Fig. 4e), tar ball (Fig.4f), organic
340 (Fig.4g), metal (Fig. 4h) and fly ash (Fig. 4i). The classification is similar to the work reported by Li and
341 Shao (2009).

342 The most common particles are sulphates and nitrates (Figs. 4a and b), which are of the size around 1.0
343 μm , and have a light scattering ability (Jacobson, 2001). Sulphates appeared as subrounded masses under
344 the TEM, which decomposed or evaporated under the electron beam exposure. Conventionally, they were
345 formed by the reaction of precursor SO_2 or H_2SO_4 with other gases or particles (Khoder, 2002). Nitrates
346 were mostly of scalloped morphology in the TEM images. They were relatively stable when exposed to the
347 electron beam. Nitrates formed through the homogeneous reaction with the precursor either NO_2 or
348 heterogenic reaction with HNO_3 (Khoder, 2002). (Pathak et al., 2004; Seinfeld and Pandis, 2012).

349 In the clear days, as the result of effects of northern air mass, dust particles were relatively abundant. The
350 size of dust particles (Fig. 4c) were large, usually bigger than 1.0 μm , so far as to 8.0 μm . Their compositions
351 differed from each other, mostly are silicates and calcium sulphate or carbonate, all of which were stable
352 under the exposure of the electron beam. Dust particles were reported to have a light scattering effect,

353 resulting in a negative aerosol radiative forcing (Wang et al., 2009b). They took up a large portion in EP-4,
354 impacted by the north wind taking along particles from the dusty regions.

355 As for the haze episode, K-rich particles (Li et al., 2010; Duan et al., 2004; Engling et al., 2009), soot (Li
356 et al., 2010), tar ball (Chakrabarty et al., 2010; Bond, 2001) and organic (Lack et al., 2012) were more
357 observed under the TEM. K-rich particles (Fig. 4d) often existed as sulphate or nitrate. A larger fraction of
358 K-rich particles was observed in EP-5 than those in the other periods. Together with the back trajectories
359 and fire spot maps, it was supposed that the regional haze occurred in EP-5 was contributed significantly
360 by the biomass burning. K-rich particles were characterized by the irregular shape, which was unstable
361 when exposed to electron beam. KCl was barely detected in the samples, even though it has been
362 recommended that KCl was internally mixed with K_2SO_4 and KNO_3 in fresh biomass burning plumes (Li
363 et al., 2010; Li et al., 2003; Adachi and Buseck, 2008). Based on the EDS data, K-rich particles in the present
364 work mostly consisted of N, Na, O, S, and K, whereas it was free of Cl, implying KCl could have suffered
365 from chemical reactions and transformed into sulphates or nitrates (Li and Shao, 2010). Such particles
366 displayed a negative climate forcing (Hauglustaine et al., 2014).

367 It was well documented that soot (Fig. 4e) was vital to light absorption, which could alter regional
368 atmospheric stability and vertical motions, the large scale circulation and precipitation with significant
369 regional climate effects (Ramanathan et al., 2001; Jacobson, 2002). It was well characterized by a structure
370 like onion ring, resembling a fractal long chain as agglomerates of small spherical monomers (Li and Shao,
371 2009). The fresh soot was loose and externally mixed. However, after undergoing a long-range
372 transportation and aging in the atmosphere, soot became more compacted, with a slight increase of O
373 concentration because of the photochemistry (Stanmore et al., 2001; [Krasowsky et al., 2016](#)). Meanwhile,
374 soot generally attached to other particles on the surface or serves as the core for other particle formation.

375 Tar ball (Fig. 4f) was present as a spherical carbon ball with a small fraction of O. It was thought to
376 origin from the smouldering combustion and have relatively strong absorption effects (Chakrabarty et al.,
377 2010; Bond, 2001). Tar balls constituted a large fraction of the fresh emitted wildfire carbonaceous particles
378 (China et al., 2013; Lack et al., 2012). But it was seldom observed in the present work, even in EP-5 when

379 there was severe biomass burning emission, which may be due to the difference in burning species and
380 conditions.

381 Organic matter (Fig. 4g) identified by HRTEM was amorphous species, and was stable under the strong
382 electron beam exposure. It could be traced to the direct emission such as biomass burning (Lack et al.,
383 2012), or the second reaction between VOCs with ozone (Wang et al., 2012a). It can absorb radiation in the
384 low-visible and UV wavelengths (Chakrabarty et al., 2010;Clarke et al., 2007;Lewis et al., 2008;Hoffer et
385 al., 2006). In addition, when compassing soot as the core, organic matter can enhance absorption by internal
386 mixing (Adachi and Buseck, 2008).

387 For the common haze and fog episodes, the stagnated weather favours the accumulation of pollutants,
388 especially metal particles and fly ash (Hu et al., 2015). Metal particles (Fig. 4h) were generally round and
389 stable under the TEM. Fly ash (Fig. 4i) was a dark sphere with large size of $> 1 \mu\text{m}$. It was a common
390 product of industrial activities in the northern China (Shi et al., 2003). As the complex refractive index
391 (CRI) indicated, metal oxide particles and fly ash can scatter light, but the former has a weak absorption
392 ability while the later has almost no light absorption ability (Ebert et al., 2004).

393 Figure 5 shows percentage of nine components in clear, haze and fog episodes under external mixing,
394 internal mixing and adjacent states (partially internal mixing). About 28% of particles were internally mixed
395 in the foggy days, while about 52% of particles exhibited external mixing state in clear days based on the
396 TEM analysis. Mineral particles were inclined to be externally mixed with K-rich particles and organic
397 matter in clear days, while the external ratio of other particles were relatively lower, particularly in the haze
398 and fog days. Li et al. (2010) showed that mineral particles generally displayed external association with
399 organic matter or other particles. However, many fine particles including metal-bearing particles, fly ash
400 and soot were often internally mixed with S-rich and K-rich particles, particularly during the fog-haze
401 episodes. Shi et al. (2008) reported that rapid aging of fresh soot tended to appear during the fog-haze days,
402 which were generally associated with ammonium sulfate. Heavy polluted air generally promoted the
403 coagulation between S/K-rich particles and those fine particles such as metal particles, soot, and fly ash (Li

404 [and Shao, 2009](#)), which could explain the results. Additionally, ~~Haze-haze~~ and fog episodes held a higher
405 possibility of collision and attachment due to the heavy particle loading and prolonged remaining in the
406 atmosphere ([Li and Shao, 2009](#); [Li et al., 2010](#)), leading to a higher internal mixed state percentage around
407 65%.

408 **3.4 The relation of optical properties and the morphologies of aerosol particles**

409 The different morphologies of the particles collected from the different weather can be easily identified
410 under the TEM, as shown in Fig. 6. Due to the washout effect of the heavy rain, the particles collected in
411 the typical clear period of EP-2 were much smaller in size (Figs. 6a, b), which was in good agreement with
412 the larger Ångström exponent. The coarse particles, such as dusts, were hardly observed, whereas a few K-
413 rich particles were detected, of which presented in small cubic shape. Such particles could be explained by
414 the coal combustion around the sampling site due to the slight fire spots presence. Besides, the cubic shape
415 of K-rich particles suggested they have not undergone long transportation or severe photochemical reaction
416 [because cubic K-rich particles were generally generated from the molten nature of the material at high](#)
417 [temperatures](#) (Ault et al., 2012). Likewise, soot was generally less oxidized in the EP2 periods, maintaining
418 fractional morphologies and externally mixed. Small metal particles and amorphous Zn-particles dominated
419 the fine particles, which was ascribed to the industrial activity and/or waste incineration (Choël et al.,
420 2006;Moffet et al., 2008).

421 In the EP-5 episode, the increased aerosol loading played a remarkable role in the enhancement of
422 scattering coefficient and decrease of visibility (Kang et al., 2013;Charlson et al., 1987;Deng et al., 2008).
423 Because of the high rate of aerosol collision, particles were larger than those in the clear days (Figs. 6c, d),
424 leading to a smaller Ångström exponent. Almost of the soot particles observed under the TEM were
425 compact and adhesive. It was internally mixed with the K-rich particles, which were larger, rounder or with
426 a coating of high S components. As discussed above, they were probably transported from the south crop
427 residual burning and undergo the ageing in the atmosphere, confirmed by the trajectories passing through
428 intense fire spots. Due to the high concentration of soot, EP-5 were characterized by a high absorption
429 coefficient, shown in Fig. 3.

430 The BC variations in the different weather types during the sampling period were illustrated in Fig. 7.
431 The preliminary component of BC could be viewed as the soot. High BC concentration was easily
432 recognized in EP-5 with a mean value of $12.8 \mu\text{g m}^{-3}$, while it is low up to $1.04 \mu\text{g m}^{-3}$ during the clear
433 periods. The former is about 11.3 times higher than that of the latter, which is due to the lower boundary
434 layer. In comparison, absorption coefficient of EP-5 (468.7 Mm^{-1}) was about 94.7 times higher than that of
435 EP-4 (1.3 Mm^{-1}), more than 8 times of the BC ratio. It was supposed that BC was internally mixed with
436 other aerosols in the EP-5, which lead to the considerable elevation of absorption coefficient (Tan et al.,
437 2016). However, Models-models estimated an enhancement of BC forcing up to a factor of 2.9 when BC is
438 internally mixed with other aerosols, compared with externally mixed scenarios (Jacobson, 2001), which
439 was much lower than this case. Accordingly, other light absorbing substances may contribute to the
440 discrepancy. For example, Brown-brown carbon is an indispensable component of biomass burning, which
441 has a strong absorption ability as well (Hoffer et al., 2006; Andreae and Gelencsér, 2006). Other particles
442 like such as dust may also contribute to the over-enhanced absorption coefficient (Yang et al., 2009). Our
443 observations were agreement with the previous studies reported by (Wang et al., 2009b; Xia et al., 2006),
444 which shows that aerosol particles under hazy weather conditions generate a positive heating effect on the
445 atmospheric column ~~(Wang et al., 2009b; Xia et al., 2006).~~

446 In the foggy days of EP-3 episode, the high PM₁₀ concentration and AOD caused significant increase of
447 scattering coefficient (Tan et al., 2016). Furthermore, metal-bearing particles and soot were internally
448 associated with some coatings including S-rich, N-rich and K-rich particles. Zhang et al. (2008) reported
449 that coating with sulphuric acid enhance the optical properties of soot aerosols. Furthermore, the collected
450 particles displayed larger size than those collected from the clear days under the TEM (Figs. 6e, f). The
451 larger size particles in the foggy days could be caused by hygroscopic growth under the high relative
452 humidity, and the collision among the overloading particles, which was likewise illustrated by the Ångström
453 exponent shown in Fig.3. Consequently, the larger particles enhance the scattering of sunlight, and lead to
454 more apparent impairment of visibility (Quan et al., 2011). Chow et al. (2002a) reported that RH also has
455 a profound impact on visibility. Some fan-like nitrate particles have inclusions which may act as the growth

带格式的: 非突出显示

456 cores or be encompassed during the hygroscopic growth. Bian et al. (2009) reported that whenever the RH
457 is elevated, its importance to AOD is substantially amplified if the particles are hygroscopic (Bian et al.,
458 2009). Li et al. (2010) found that soot particles became hydrophilic when they were coated with the water-
459 soluble compounds such as sulphates or nitrates, implying that soot can provide important nuclei for the
460 development of aerosol particles. Furthermore, Fig. 6e and f illustrate a large fraction of internally mixed
461 soot. It was not visible until being exposed to electron beam for a short time. As for an internally mixed
462 particle, sulphate and nitrate coatings act as a “focusing mirror”, and enhanced light absorption greatly.
463 Therefore, the BC concentration in foggy conditions was $6.12 \mu\text{g m}^{-3}$, and the absorption coefficient is 143.7
464 Mm^{-1} , which were 2.09 and 0.83 times of the hazy days, respectively. Model calculation also have
465 recommended that light absorption ability of the internally mixed soot particles were enhanced by 30%
466 than that of soot alone (Fuller et al., 1999). A variety of metal particles were also observed in the foggy
467 days, as foggy days had a stable low upper layer boundary and slight wind, leading to the accumulation of
468 pollutions. These pollution sources range from steel plants and waste incineration to vehicle emission and
469 so on (Hu et al., 2015).

470 **4 Conclusions**

471 The relationship between characteristics of aerosol particles and optical properties is of importance to
472 the atmospheric chemistry research. However, the relationship between characteristics of aerosol particles
473 and optical absorption remains poorly understood. Characteristics of aerosol optical properties,
474 morphologies and their relationship were studied in urban Beijing during the clear, haze and fog episodes,
475 sampled from 24th May to 22nd Jun, 2012. Transmission Electron Microscope (TEM), a Cavity Ring Down
476 Spectrometer (CRDS), a nephelometer and an aethalometer were employed to investigate the corresponding
477 changes of the aerosol properties. Five episodes were categorised according to the meteorological
478 conditions and composition. The results indicated that the clear episode (EP-2 and EP-4) was characterized
479 as the low aerosol Optical Depth ($\text{AOD} = 0.72$) and less pollutants compared with haze (1.14) and fog (2.92)
480 episodes, which are mostly externally mixed. The high Ångström exponent (> 2.0) suggests that coarse
481 particles were scarcely observed in EP-2 due to the washout of a previous heavy rain, whereas they were

482 widespread in EP-4 (Ångström exponent = 0.04), which had some mineral particles introduced from the
483 north. In contrast, industry-induced haze (EP-1) and biomass burning-induced haze (EP-5) were both
484 affected by the south air mass. Higher AOD values illustrated heavy loading particle concentrations. All of
485 the particles were classified into nine categories including S-rich, N-rich, mineral, K-rich, soot, tar ball,
486 organic, metal and fly ash based on the TEM analysis. In the haze episode, as the influence of severe crop
487 residue combustion, a large fraction of soot was detected, which sticks to sulphate or nitrate particles
488 transformed from KCl. Both black carbon (BC) acceleration, internally mixed effects, and other light
489 absorbing substances, contributed the light absorption enhancement. For foggy days, soot was mostly
490 internally mixed with sulphates and nitrates, which revealed themselves after electron exposure under the
491 TEM. The larger size distribution was likely to be caused by both hygroscopic growth and collision between
492 particles during the aging. About 28% of particles were internally mixed in the foggy days, which favored
493 the light absorption. The comparison of all the episodes provides a deeper insight of how mixing states
494 influence the aerosol extinction properties and also a clue to the air pollution control in the crop burning
495 seasons. The result presented herein is beneficial to air pollution control and prevention in China.

496 **ACKNOWLEDGMENTS**

497 This work was supported by National Natural Science Foundation of China (Nos. 21577022, 21190053,
498 40975074), Ministry of Science and Technology of China (2016YFC0202700), and International
499 cooperation project of Shanghai municipal government (15520711200).

500 **References**

- 501 Adachi, K., and Buseck, P.: Internally mixed soot, sulfates, and organic matter in aerosol particles from
502 Mexico City, Atmos. Chem. Phys., 8, 6469-6481, 2008.
- 503 Adler, G., Riziq, A. A., Erlick, C., and Rudich, Y.: Effect of intrinsic organic carbon on the optical
504 properties of fresh diesel soot, P. Natl. Acad. Sci. USA., 107, 6699-6704, 2010.
- 505 Alexander, D. T., Crozier, P. A., and Anderson, J. R.: Brown carbon spheres in East Asian outflow and
506 their optical properties, Science, 321, 833-836, 2008.

带格式的: 字体: 11 磅

507 Anderson, T. L., and Ogren, J. A.: Determining aerosol radiative properties using the TSI 3563 integrating
508 nephelometer, *Aerosol Air Qual. Res.*, 29, 57-69, 1998.

509 Andreae, M., and Gelencsér, A.: Black carbon or brown carbon? The nature of light-absorbing
510 carbonaceous aerosols, *Atmos. Chem. Phys.*, 6, 3131-3148, 2006.

511 Ault A.P., Peters T.M., Sawvel E.J., Casuccio G.S., Willis R.D., Norris G.A., et al.: Single-particle SEM-
512 EDX analysis of iron-containing coarse particulate matter in an urban environment: sources and distribution
513 of iron within Cleveland, Ohio. *Environ Sci Technol.*, 46: 4331–4339, 2012.

514 Bahadur, R., Praveen, P. S., Xu, Y., and Ramanathan, V.: Solar absorption by elemental and brown carbon
515 determined from spectral observations, *P. Natl. Acad. Sci. USA.*, 109, 17366-17371, 2012.

516 Bian, H., Chin, M., Rodriguez, J., Yu, H., Penner, J. E., and Strahan, S.: Sensitivity of aerosol optical
517 thickness and aerosol direct radiative effect to relative humidity, *Atmos. Chem. Phys.*, 9, 2375-2386, 2009.

518 Bond, T. C.: Spectral dependence of visible light absorption by carbonaceous particles emitted from coal
519 combustion, *Geophys. Res. Lett.*, 28, 4075-4078, 2001.

520 Brown, A.J.: Spectral bluing induced by small particles under the Mie and Rayleigh regimes, *Lcarus.*, 239,
521 85-95, 2014.

522 Buseck, P. R., and POSfai, M.: Airborne minerals and related aerosol particles: Effects on climate and the
523 environment, *P. Natl. Acad. Sci. USA.*, 96, 3372-3379, 1999.

524 Carabali, G., Mamani-Paco, R., Castro, T., Peralta, O., Herrera, E., and Trujillo, B.: Optical properties,
525 morphology and elemental composition of atmospheric particles at T1 supersite on MILAGRO campaign,
526 *Atmos. Chem. Phys.*, 12, 2747-2755, 2012.

527 Chakrabarty, R., Moosmüller, H., Chen, L.-W., Lewis, K., Arnott, W., Mazzoleni, C., Dubey, M., Wold,
528 C., Hao, W., and Kreidenweis, S.: Brown carbon in tar balls from smoldering biomass combustion, *Atmos.*
529 *Chem. Phys.*, 10, 6363-6370, 2010.

530 Chameides, W. L., Yu, H., Liu, S., Bergin, M., Zhou, X., Mearns, L., Wang, G., Kiang, C., Saylor, R., and
531 Luo, C.: Case study of the effects of atmospheric aerosols and regional haze on agriculture: An opportunity

带格式的: 字体: 11 磅

带格式的: 字体: 11 磅

532 to enhance crop yields in China through emission controls?, *P. Natl. Acad. Sci. USA.*, 96, 13626-13633,
533 1999.

534 Charlson, R. J., Lovelock, J. E., Andreae, M. O., and Warren, S. G.: Oceanic phytoplankton, atmospheric
535 sulphur, cloud albedo and climate, *Nature*, 326, 655-661, 1987.

536 Che, H., Xia, X., Zhu, J., Li, Z., Dubovik, O., Holben, B., Goloub, P., Chen, H., Estelles, V., and Cuevas-
537 Agulló, E.: Column aerosol optical properties and aerosol radiative forcing during a serious haze-fog month
538 over North China Plain in 2013 based on ground-based sunphotometer measurements, *Atmos. Chem. Phys.*,
539 14, 2125-2138, 2014.

540 China, S., Mazzoleni, C., Gorkowski, K., Aiken, A. C., and Dubey, M. K.: Morphology and mixing state
541 of individual freshly emitted wildfire carbonaceous particles, *Nature commun.*, 4, 2013.

542 Choël, M., Deboudt, K., Flament, P., Lecomte, G., Perdrix, E., and Sobanska, S.: Fast evolution of
543 tropospheric Pb-and Zn-rich particles in the vicinity of a lead smelter, *Atmos. Environ.*, 40, 4439-4449,
544 2006.

545 Chow, J. C., Bachmann, J. D., Wierman, S. S., Mathai, C., Malm, W. C., White, W. H., Mueller, P. K.,
546 Kumar, N., and Watson, J. G.: Visibility: science and regulation, *J. Air. Waste Manage.*, 52, 973-999, 2002.

547 Clarke, A., McNaughton, C., Kapustin, V., Shinozuka, Y., Howell, S., Dibb, J., Zhou, J., Anderson, B.,
548 Brekhovskikh, V., and Turner, H.: Biomass burning and pollution aerosol over North America: Organic
549 components and their influence on spectral optical properties and humidification response, *J. Geophys.*
550 *Res.-Atmos.*, 112, 2007.

551 Deng, X., Tie, X., Wu, D., Zhou, X., Bi, X., Tan, H., Li, F., and Jiang, C.: Long-term trend of visibility and
552 its characterizations in the Pearl River Delta (PRD) region, China, *Atmos. Environ.*, 42, 1424-1435, 2008.

553 Dey, S., Tripathi, S. N., Singh, R. P., and Holben, B. N.: Influence of dust storms on the aerosol optical
554 properties over the Indo-Gangetic basin, *J. Geophys. Res.-Atmos.*, 109, 10.1029/2004jd004924, 2004.

555 Doran, J., Barnard, J. C., Arnott, W., Cary, R., Coulter, R., Fast, J. D., Kassianov, E. I., Kleinman, L.,
556 Laulainen, N. S., and Martin, T.: The T1-T2 study: evolution of aerosol properties downwind of Mexico
557 City, *Atmos. Chem. Phys.*, 7, 1585-1598, 2007.

558 Duan, F., Liu, X., Yu, T., and Cachier, H.: Identification and estimate of biomass burning contribution to
559 the urban aerosol organic carbon concentrations in Beijing, *Atmos. Environ.*, 38, 1275-1282, 2004.

560 Ebert, M., Weinbruch, S., Hoffmann, P., and Ortner, H. M.: The chemical composition and complex
561 refractive index of rural and urban influenced aerosols determined by individual particle analysis, *Atmos.*
562 *Environ.*, 38, 6531-6545, 2004.

563 Eck, T. F., Holben, B. N., Reid, J. S., Dubovik, O., Smirnov, A., O'Neill, N. T., Slutsker, I., and Kinne, S.:
564 Wavelength dependence of the optical depth of biomass burning, urban, and desert dust aerosols, *J.*
565 *Geophys. Res.-Atmos.*, 104, 31333-31349, 10.1029/1999jd900923, 1999.

566 Engling, G., Lee, J. J., Tsai, Y.-W., Lung, S.-C. C., Chou, C. C.-K., and Chan, C.-Y.: Size-resolved
567 anhydrosugar composition in smoke aerosol from controlled field burning of rice straw, *Aerosol Air Qual.*
568 *Res.*, 43, 662-672, 2009.

569 Fu, H., Zhang, M., Li, W., Chen, J., Wang, L., Quan, X., and Wang, W.: Morphology, composition and
570 mixing state of individual carbonaceous aerosol in urban Shanghai, *Atmos. Chem. Phys.*, 12, 693-707, 2012.

571 Fuller, K. A., Malm, W. C., and Kreidenweis, S. M.: Effects of mixing on extinction by carbonaceous
572 particles, *J. Geophys. Res.-Atmos.*, 104, 15941-15954, 1999.

573 Guo, L., Hu, Y., Hu, Q., Lin, J., Li, C., Chen, J., Li, L., and Fu, H.: Characteristics and chemical
574 compositions of particulate matter collected at the selected metro stations of Shanghai, China, *Sci. Total*
575 *Environ.*, 496, 443-452, 2014a.

576 Guo, Y., Feng, N., Christopher, S. A., Kang, P., Zhan, F. B., and Hong, S.: Satellite remote sensing of fine
577 particulate matter (PM_{2.5}) air quality over Beijing using MODIS, *Int. J. Remote Sens.*, 35, 6522-6544, 2014b.

578 Gustafsson, Ö., Krusá, M., Zencak, Z., Sheesley, R. J., Granat, L., Engström, E., Praveen, P., Rao, P., Leck,
579 C., and Rodhe, H.: Brown clouds over South Asia: biomass or fossil fuel combustion?, *Science*, 323, 495-
580 498, 2009.

581 Habib, G., Venkataraman, C., Bond, T. C., and Schauer, J. J.: Chemical, microphysical and optical
582 properties of primary particles from the combustion of biomass fuels, *Environ. Sci. Technol.*, 42, 8829-
583 8834, 2008.

584 Hand, J. L., Malm, W., Laskin, A., Day, D., Lee, T.-b., Wang, C., Carrico, C., Carrillo, J., Cowin, J. P., and
585 Collett, J.: Optical, physical, and chemical properties of tar balls observed during the Yosemite Aerosol
586 Characterization Study, *J. Geophys. Res.-Atmos.*, 110, 2005.

587 Hansen, A.: *The Aethalometer Manual*, Magee Sci., Berkeley, Calif, 2003.

588 Hoffer, A., Gelencsér, A., Guyon, P., Kiss, G., Schmid, O., Frank, G., Artaxo, P., and Andreae, M.: Optical
589 properties of humic-like substances (HULIS) in biomass-burning aerosols, *Atmos. Chem. Phys.*, 6, 3563-
590 3570, 2006.

591 Hu, Y., Lin, J., Zhang, S., Kong, L., Fu, H., and Chen, J.: Identification of the typical metal particles among
592 haze, fog, and clear episodes in the Beijing atmosphere, *Sci. Total Environ.*, 511, 369-380, 2015.

593 Hauglustaine, D.A., Balkanski, Y., Schulz, M.: A global model simulation of present and future nitrate
594 aerosols and their direct radiative forcing of climate, *Atmos. Chem. Phys.*, 14, 6863-6949, 2014.

595 Jacobson, M. Z.: Strong radiative heating due to the mixing state of black carbon in atmospheric aerosols,
596 *Nature*, 409, 695-697, 2001.

597 Jacobson, M. Z.: Control of fossil - fuel particulate black carbon and organic matter, possibly the most
598 effective method of slowing global warming, *J. Geophys. Res.-Atmos.*, 107, ACH 16-11-ACH 16-22, 2002.

599 Jeong, C.-H., Hopke, P. K., Kim, E., and Lee, D.-W.: The comparison between thermal-optical
600 transmittance elemental carbon and Aethalometer black carbon measured at multiple monitoring sites,
601 *Atmos. Environ.*, 38, 5193-5204, 2004.

602 Kang, H., Zhu, B., Su, J., Wang, H., Zhang, Q., and Wang, F.: Analysis of a long-lasting haze episode in
603 Nanjing, China, *Atmos. Res.*, 120, 78-87, 2013.

604 [Krasowsky, T.S., McMeeking, G.R., Wang, D.B., Sioutas, C., Ban-Weiss, G.A.: Measurements of the](#)
605 [impact of atmospheric aging on physical and optical properties of ambient black carbon particles in Los](#)
606 [Angeles, *Atmos. Environ.*, 142, 496-504, 2016.](#)

607 Katrinak, K. A., Rez, P., Perkes, P. R., and Buseck, P. R.: Fractal geometry of carbonaceous aggregates
608 from an urban aerosol, *Environ. Sci. Technol.*, 27, 539-547, 1993.

带格式的: 字体: 11 磅

609 Khoder, M.: Atmospheric conversion of sulfur dioxide to particulate sulfate and nitrogen dioxide to
610 particulate nitrate and gaseous nitric acid in an urban area, *Chemosphere*, 49, 675-684, 2002.

611 Kleinman, L. I., Daum, P. H., Lee, Y. N., Senum, G. I., Springston, S. R., Wang, J., Berkowitz, C., Hubbe,
612 J., Zaveri, R. A., and Brechtel, F. J.: Aircraft observations of aerosol composition and ageing in New
613 England and Mid - Atlantic States during the summer 2002 New England Air Quality Study field campaign,
614 *J. Geophys. Res.-Atmos.*, 112, 2007.

615 Lack, D. A., Langridge, J. M., Bahreini, R., Cappa, C. D., Middlebrook, A. M., and Schwarz, J. P.: Brown
616 carbon and internal mixing in biomass burning particles, *P. Natl. Acad. Sci. USA.*, 109, 14802-14807,
617 10.1073/pnas.1206575109, 2012.

618 Langridge, J. M., Lack, D., Brock, C. A., Bahreini, R., Middlebrook, A. M., Neuman, J. A., Nowak, J. B.,
619 Perring, A. E., Schwarz, J. P., and Spackman, J. R.: Evolution of aerosol properties impacting visibility and
620 direct climate forcing in an ammonia - rich urban environment, *J. Geophys. Res.-Atmos.*, 117, 2012.

621 Lei, T., Zuend, A., Wang, W., Zhang, Y., and Ge, M.: Hygroscopicity of organic compounds from biomass
622 burning and their influence on the water uptake of mixed organic–ammonium sulfate aerosols, *Atmos.*
623 *Chem. Phys.*, 14, 11625-11663, 2014.

624 Lewis, K., Arnott, W. P., Moosmüller, H., and Wold, C. E.: Strong spectral variation of biomass smoke
625 light absorption and single scattering albedo observed with a novel dual - wavelength photoacoustic
626 instrument, *J. Geophys. Res.-Atmos.*, 113, 2008.

627 Li, C., Marufu, L. T., Dickerson, R. R., Li, Z., Wen, T., Wang, Y., Wang, P., Chen, H., and Stehr, J. W.: In
628 situ measurements of trace gases and aerosol optical properties at a rural site in northern China during East
629 Asian Study of Tropospheric Aerosols: An International Regional Experiment 2005, *J. Geophys. Res.-*
630 *Atmos.*, 112, 2007.

631 Li, J., Pósfai, M., Hobbs, P. V., and Buseck, P. R.: Individual aerosol particles from biomass burning in
632 southern Africa: 2, Compositions and aging of inorganic particles, *J. Geophys. Res.-Atmos.*, 108, 2003.

633 Li, W., and Shao, L.: Transmission electron microscopy study of aerosol particles from the brown hazes in
634 northern China, *J. Geophys. Res.-Atmos.*, 114, 2009.

635 Li, W., and Shao, L.: Direct observation of aerosol particles in aged agricultural biomass burning plumes
636 impacting urban atmospheres, *Atmos. Chem. Phys.*, 10, 10589-10623, 2010.

637 Li, W., Shao, L., and Buseck, P.: Haze types in Beijing and the influence of agricultural biomass burning,
638 *Atmos. Chem. Phys.*, 10, 8119-8130, 2010.

639 [Li, W., Shao, L.: Characterization of mineral particles in winter fog of Beijing analyzed by TEM and SEM.](#)
640 [*Environ. Monit. Assess.*, 161, 565-573, 2010.](#)

641 Moffet, R. C., Desyaterik, Y., Hopkins, R. J., Tivanski, A. V., Gilles, M. K., Wang, Y., Shutthanandan, V.,
642 Molina, L. T., Abraham, R. G., and Johnson, K. S.: Characterization of aerosols containing Zn, Pb, and Cl
643 from an industrial region of Mexico City, *Environ. Sci. Technol.*, 42, 7091-7097, 2008.

644 Moffet, R. C., and Prather, K. A.: In-situ measurements of the mixing state and optical properties of soot
645 with implications for radiative forcing estimates, *P. Natl. Acad. Sci. USA.*, 106, 11872-11877, 2009.

646 Pathak, R. K., Yao, X., and Chan, C. K.: Sampling artifacts of acidity and ionic species in PM_{2.5}, *Environ.*
647 *Sci. Technol.*, 38, 254-259, 2004.

648 Peppler, R., Bahrmann, C., Barnard, J. C., Laulainen, N., Turner, D., Campbell, J., Hlavka, D., Cheng, M.,
649 Ferrare, R., and Halthore, R.: ARM Southern Great Plains site observations of the smoke pall associated
650 with the 1998 Central American fires, *B. Am. Meteorol. Soc.*, 81, 2563-2591, 2000.

651 Qian, Y., Wang, W., Leung, L. R., and Kaiser, D. P.: Variability of solar radiation under cloud - free skies
652 in China: The role of aerosols, *Geophys. Res. Lett.*, 34, 2007.

653 Quan, J., Zhang, Q., He, H., Liu, J., Huang, M., and Jin, H.: Analysis of the formation of fog and haze in
654 North China Plain (NCP), *Atmos. Chem. Phys.*, 11, 8205-8214, 2011.

655 Ram, K., Sarin, M., and Tripathi, S.: Temporal trends in atmospheric PM_{2.5}, PM₁₀, elemental carbon,
656 organic carbon, water-soluble organic carbon, and optical properties: impact of biomass burning emissions
657 in the Indo-Gangetic Plain, *Environ. Sci. Technol.*, 46, 686-695, 2012.

带格式的: 字体: 11 磅

658 Ramana, M., Ramanathan, V., Feng, Y., Yoon, S., Kim, S., Carmichael, G., and Schauer, J.: Warming
659 influenced by the ratio of black carbon to sulphate and the black-carbon source, *Nat. Geosci.*, 3, 542-545,
660 2010.

661 Ramanathan, V., Crutzen, P. J., Lelieveld, J., Mitra, A., Althausen, D., Anderson, J., Andreae, M., Cantrell,
662 W., Cass, G., and Chung, C.: Indian Ocean Experiment: An integrated analysis of the climate forcing and
663 effects of the great Indo-Asian haze, 2001.

664 Ramanathan, V., Chung, C., Kim, D., Bettge, T., Buja, L., Kiehl, J., Washington, W., Fu, Q., Sikka, D.,
665 and Wild, M.: Atmospheric brown clouds: Impacts on South Asian climate and hydrological cycle, *P. Natl.*
666 *Acad. Sci. USA.*, 102, 5326-5333, 2005.

667 Ramanathan, V., Ramana, M. V., Roberts, G., Kim, D., Corrigan, C., Chung, C., and Winker, D.: Warming
668 trends in Asia amplified by brown cloud solar absorption, *Nature*, 448, 575-578, 2007.

669 Roden, C. A., Bond, T. C., Conway, S., and Pinel, A. B. O.: Emission factors and real-time optical
670 properties of particles emitted from traditional wood burning cookstoves, *Environ. Sci. Technol.*, 40, 6750-
671 6757, 2006.

672 [Saleh, R., Adams, P.J., Donahue, N.M., Robinson, A.L.: The interplay between assumed morphology and](#)
673 [the direct radiative effect of light-absorbing organic aerosol, *Geophys. Res. Lett.* 43, 8735–8743, 2016.](#)

674 Seinfeld, J. H., and Pandis, S. N.: Atmospheric chemistry and physics: from air pollution to climate change,
675 John Wiley & Sons, 2012.

676 Shi, Z., Shao, L., Jones, T. P., Whittaker, A., Lu, S., Berube, K. A., He, T., and Richards, R. J.:
677 Characterization of airborne individual particles collected in an urban area, a satellite city and a clean air
678 area in Beijing, 2001, *Atmos. Environ.*, 37, 4097-4108, 2003.

679 [Shi, Z. B., D. Z. Zhang, H. Z. Ji, S. Hasegawa, and M. Hayashi.: Modification of soot by volatile species](#)
680 [in an urban atmosphere, *Sci. Total Environ.*, 389, 195–201, 2008.](#)

681 [Shingler, T., Sorooshian, A., Ortega, A., Crosbie, E., Wonaschütz, A., Perring, A.E.: Ambient observations](#)
682 [of hygroscopic growth factor and f\(RH\) below 1: Case studies from surface and airborne measurements, *J.*](#)
683 [Geophys. Res., 121, 13661-13677, 2016.](#)

带格式的: 字体: 11 磅

684 Solomon, S.: Climate change 2007-the physical science basis: Working group I contribution to the fourth
685 assessment report of the IPCC, Cambridge University Press, 2007.

686 Stanmore, B., Brilhac, J., and Gilot, P.: The oxidation of soot: a review of experiments, mechanisms and
687 models, Carbon, 39, 2247-2268, 2001.

688 Sun, Y., Zhuang, G., Tang, A., Wang, Y., and An, Z.: Chemical characteristics of PM_{2.5} and PM₁₀ in haze-
689 fog episodes in Beijing, Environ. Sci. Technol., 40, 3148-3155, 2006.

690 Takemura, T., Nakajima, T., Dubovik, O., Holben, B. N., and Kinne, S.: Single-scattering albedo and
691 radiative forcing of various aerosol species with a global three-dimensional model, J. Climate., 15, 333-
692 352, 2002.

693 [Tan, H.B., Liu, L., Fan, S.J., Li, F., Yin, Y., Cai, M.F., Chan, P.W., 2016. Aerosol optical properties and
694 mixing state of black carbon in the Pearl River Delta, China, Atmos. Environ., 131, 196-208, 2016.](#)

695 Wang, G., Kawamura, K., Xie, M., Hu, S., Cao, J., An, Z., Waston, J. G., and Chow, J. C.: Organic
696 molecular compositions and size distributions of Chinese summer and autumn aerosols from Nanjing:
697 Characteristic haze event caused by wheat straw burning, Environ. Sci. Technol., 43, 6493-6499, 2009a.

698 Wang, H., He, C., Morawska, L., McGarry, P., and Johnson, G.: Ozone-initiated particle formation, particle
699 aging, and precursors in a laser printer, Environ. Sci. Technol., 46, 704-712, 2012a.

700 Wang, R., Tao, S., Wang, W., Liu, J., Shen, H., Shen, G., Wang, B., Liu, X., Li, W., and Huang, Y.: Black
701 carbon emissions in China from 1949 to 2050, Environ. Sci. Technol., 46, 7595-7603, 2012b.

702 Wang, X., and Chen, J.: Fog Formation in Cold Season in Ji’nan, China: Case Analyses with
703 Application of HYSPLIT Model, Adv. Meteorol., 2014, 8, 10.1155/2014/940956, 2014.

704 Wang, X., Xu, B., and Ming, J.: An overview of the studies on black carbon and mineral dust deposition in
705 snow and ice cores in East Asia, J. Meteorol. Res., 28, 354-370, 10.1007/s13351-014-4005-7, 2014.

706 Wang, Y., Zhuang, G., Sun, Y., and An, Z.: The variation of characteristics and formation mechanisms of
707 aerosols in dust, haze, and clear days in Beijing, Atmos. Environ., 40, 6579-6591, 2006.

708 Wang, Y., Che, H., Ma, J., Wang, Q., Shi, G., Chen, H., Goloub, P., and Hao, X.: Aerosol radiative forcing
709 under clear, hazy, foggy, and dusty weather conditions over Beijing, China, Geophys. Res. Lett., 36, 2009b.

带格式的: 字体: 11 磅, 下标

带格式的: 字体: 11 磅

710 Wu, D., Mao, J., Deng, X., Tie, X., Zhang, Y., Zeng, L., Li, F., Tan, H., Bi, X., and Huang, X.: Black
711 carbon aerosols and their radiative properties in the Pearl River Delta region, *Science in China Series D:
712 Earth Sciences*, 52, 1152-1163, 2009.

713 Xia, X., Chen, H., Wang, P., Zhang, W., Goloub, P., Chatenet, B., Eck, T., and Holben, B.: Variation of
714 column - integrated aerosol properties in a Chinese urban region, *J. Geophys. Res.-Atmos.*, 111, 2006.

715 Yan, P., Tang, J., Huang, J., Mao, J., Zhou, X., Liu, Q., Wang, Z., and Zhou, H.: The measurement of
716 aerosol optical properties at a rural site in Northern China, *Atmos. Chem. Phys.*, 8, 2229-2242, 2008.

717 Yang, M., Howell, S., Zhuang, J., and Huebert, B.: Attribution of aerosol light absorption to black carbon,
718 brown carbon, and dust in China—interpretations of atmospheric measurements during EAST-AIRE, *Atmos.
719 Chem. Phys.*, 9, 2035-2050, 2009.

720 Yu, X., Cheng, T., Chen, J., and Liu, Y.: A comparison of dust properties between China continent and
721 Korea, Japan in East Asia, *Atmos. Environ.*, 40, 5787-5797, 2006.

722 Zhang, R., Khalizov, A. F., Pagels, J., Zhang, D., Xue, H., and McMurry, P. H.: Variability in morphology,
723 hygroscopicity, and optical properties of soot aerosols during atmospheric processing, *P. Natl. Acad. Sci.
724 USA.*, 105, 10291-10296, 2008.

725 Zhang, W., Zhuang, G., Guo, J., Xu, D., Wang, W., Baumgardner, D., Wu, Z., and Yang, W.: Sources of
726 aerosol as determined from elemental composition and size distributions in Beijing, *Atmos. Res.*, 95, 197-
727 209, <http://dx.doi.org/10.1016/j.atmosres.2009.09.017>, 2010.

728

729

730

731 **Table 1** Details about the analysed samples on the sampling time, instantaneous meteorological state and
 732 the number of particle analysed in each sample.

Sampling Time (BST ^a)			Conditions	RH (%)	Temp. (°C)	Wind		Visibility (km)	No.
Date	Starting	Duration				Speed (m/s)	Direction		
25-05-2012	13:40	4 min	Clear	20	29	2	160	-	136
30-05-2012	9:31	16 min	Clear	29	24	7	350	-	92
02-06-2012	9:00	1 min	Mist ^b	83	20	4	180	2	146
02-06-2012	13:27	2 min	Clear	48	27	4	190	-	138
03-06-2012	10:13	15 s	Fog	88	22	1	variable	1.2	110
18-06-2012	18:52	2 min	Haze	55	29	3	140	3	172
19-06-2012	9:10	2 min	Haze	61	25	1	variable	2.8	120
21-06-2012	9:10	1 min	Haze	69	26	2	110	2.2	117
23-06-2012	12:45	2 min	Mist ^b	84	25	4	120	3	142

^aBeijing standard time (8 h prior to GMT).

^bMist is studied here as fog.

733

734

735 **Figure captions**

736 **Figure 1.** 5 episodes categorization. EP-1 features haze induced mainly from transportation of south
737 industrial pollution, EP-2 clear, EP-3 frequent transition among haze, fog and clear conditions, EP-4 clear
738 with rain interrupted, and EP-5 haze resulted mainly from the biomass burning.

739 **Figure 2.** The 3-day back-trajectory clusters of each episode, arriving at Beijing at the height of 100 m,
740 together with the fire spot distribution of these periods.

741 **Figure 3.** TEM typical views of the particles in clear (upper panel), haze (middle panel) and fog episodes
742 (bottom panel). 9 components are marked with the colourful arrows. (a1) (b1) (c1) (d1) (e1) (f1) is obtained
743 before the electron exposure and (a2) (b2) (c2) (d2) (e2) (f2) is after exposure. A fraction of S-rich particles
744 and other unstable particles decompose after electron exposure.

745 **Figure 4.** 9 categories of particles under the TEM view. The inserted spectra are obtained by the EDS, and
746 the grid like images are acquired from the SAED. (a) S-rich, (b) N-rich, (c) mineral, (d) K-rich, (e) soot, (f) tar
747 ball, (g) organic, (h) metal, (i) fly ash.

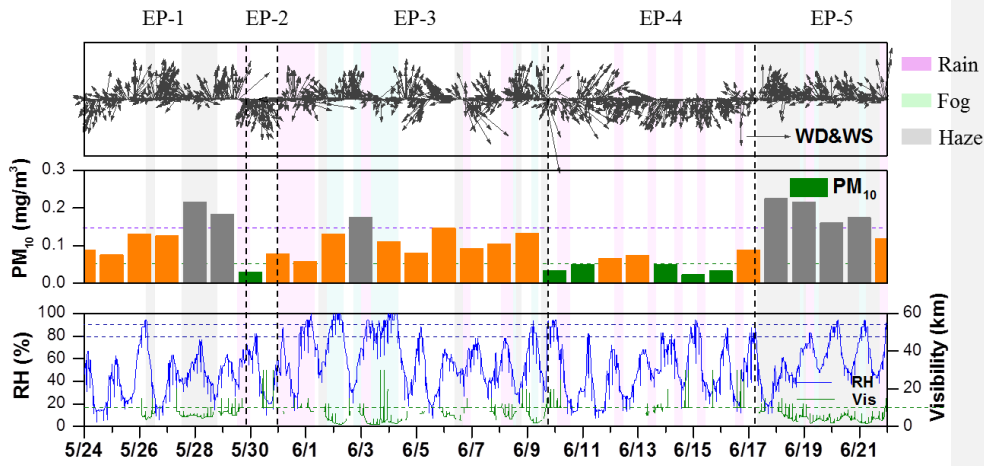
748 **Figure 5.** Variation of optical parameters during the study period. (a) Total Aerosol optical depth (AOD),
749 and AOD resulted from Mie scatter and Rayleigh scatter; (b) Ångström exponent (\AA) computed from the
750 pairs of 700 nm and 450 nm, 700 nm and 550 nm, and 550 nm and 450 nm; (c) light extinction, absorption
751 and scattering coefficients; (d) calculated single scattering albedo (SSA).

752 **Figure 6.** Percentages of 9 particle components under clear, haze and fog conditions with different mixing
753 states.

754 **Figure 7.** BC concentrations converted from the data measured by AE-31 and MAAP. Good correlation is
755 observed.

756

757



758

759

760

761

762

763

764

765

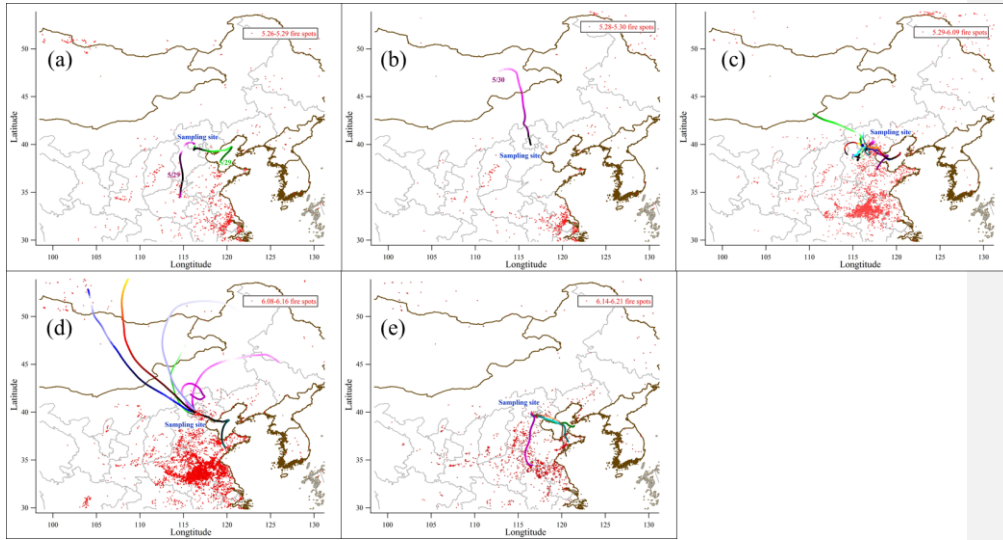
766

767

768

769

Figure 1



770

771

772

773

774

775

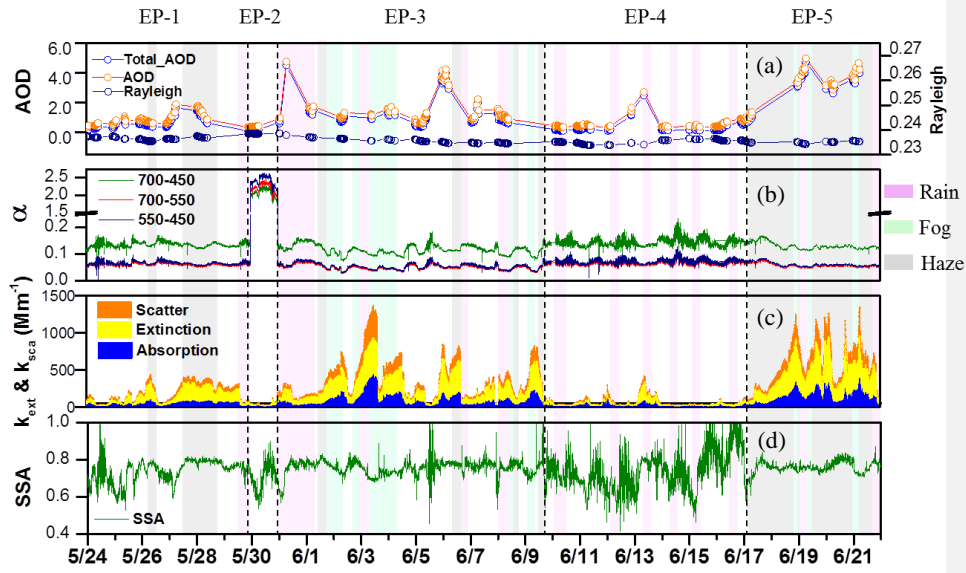
776

777

Figure 2

778

779



780

781

782

783

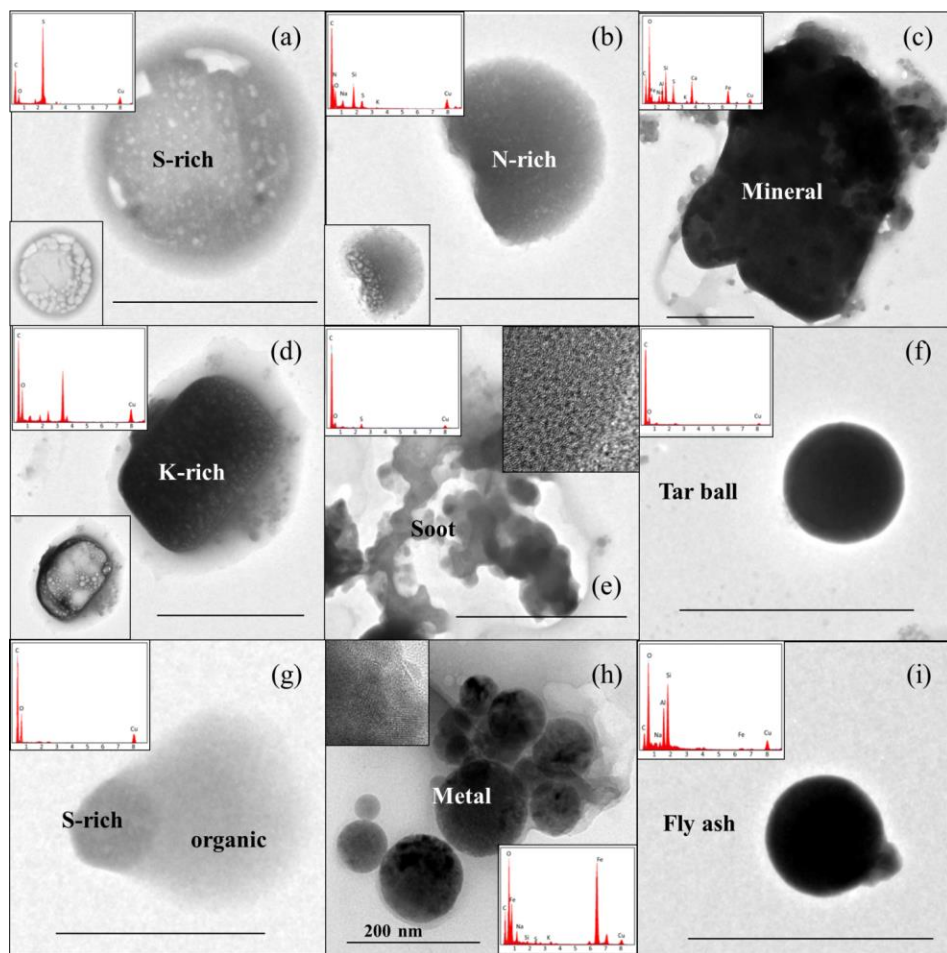
784

785

786

Figure 3

787



788

789

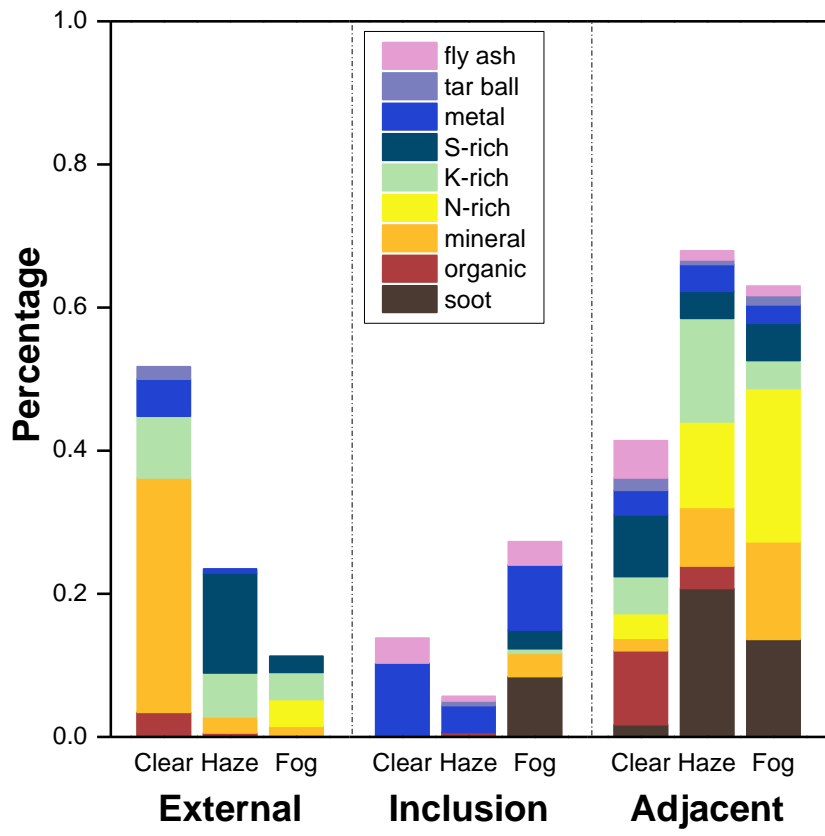
790

791

792

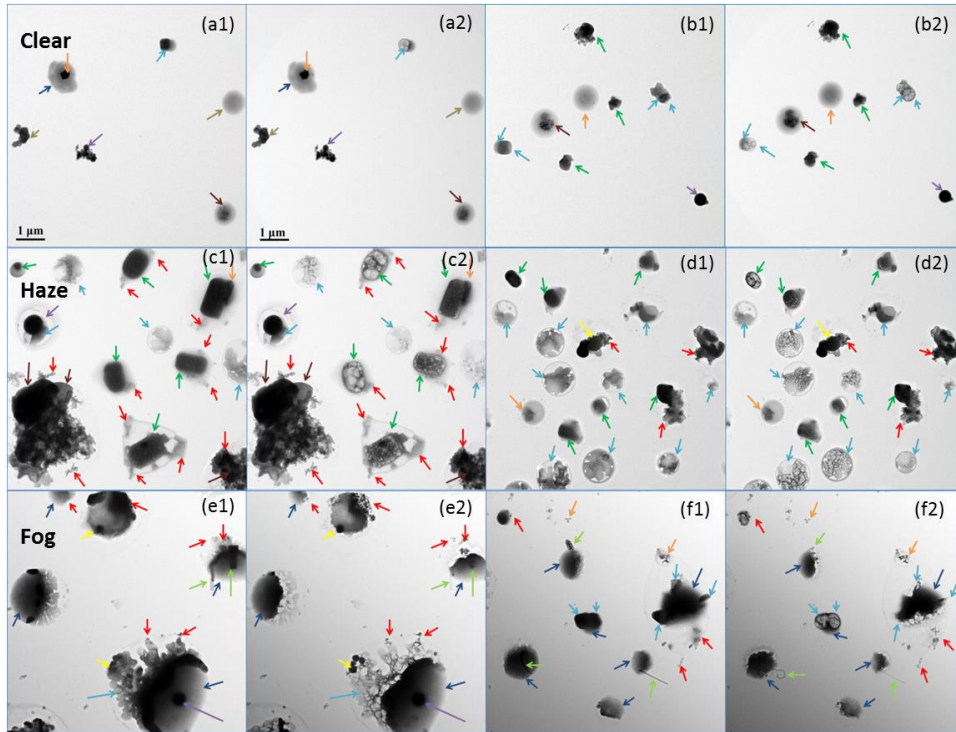
793

Figure 4



794
795
796
797

Figure 5



K-rich → S-rich → soot → fly ash → metal →
 Ca-S → tar ball → N-rich → rod → organic →

798

799

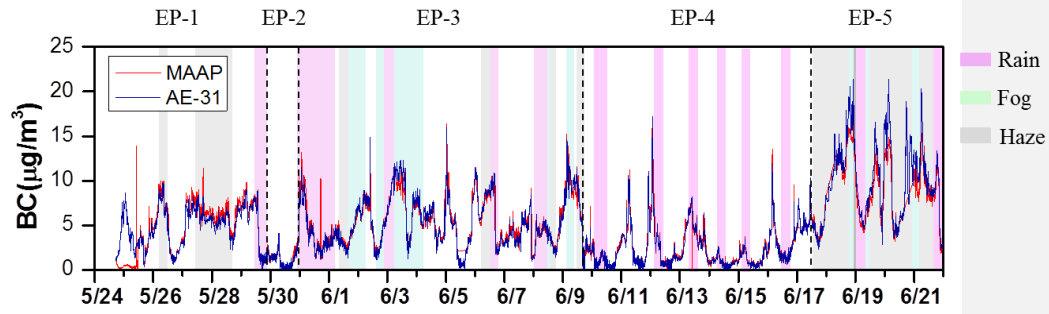
800

801

802

803

Figure 6



804
 805
 806
 807
 808
 809
 810
 811
 812
 813
 814

Figure 7